Article

Microstructure, Electromagnetic Properties, and Microwave Absorption Mechanism of SiO₂-MnO-Al₂O₃ Based Manganese Ore Powder for Electromagnetic Protection

Rui Cai [1,†]**, Wei Zheng** [2,†]**, Pingan Yang** [1,*]⬤**, Jinsong Rao** [3]**, Xin Huang** [1]**, Dashuang Wang** [3]**, Zhilan Du** [3]**, Kexin Yao** [3] **and Yuxin Zhang** [3,*]⬤

1   School of Automation, Chongqing University of Posts and Telecommunications, Chongqing 400065, China; crrrui@163.com (R.C.); huangxin@cqupt.edu.cn (X.H.)
2   China Academy of Space Technology (Xi'an), Institute of Space Antenna, Xi'an 710100, China; zhidaoyuan@163.com
3   College of Material Science and Engineering, Chongqing University, Chongqing 400044, China; rjs@cqu.edu.cn (J.R.); 20210901021@cqu.edu.cn (D.W.); 202109021015@cqu.edu.cn (Z.D.); kexinyao@cqu.edu.cn (K.Y.)
*   Correspondence: yangpa@cqupt.edu.cn (P.Y.); zhangyuxin@cqu.edu.cn (Y.Z.)
†   These authors contributed equally to this work.

Abstract: Considering the electromagnetic protection needs of important ground buildings, exploring the electromagnetic wave (EMW) absorption performance of manganese ore powder (MOP) building materials is an effective way to overcome its low added value and difficulty in popularizing. Here, choosing filling ratios commonly used in building materials such as autoclaved bricks, MOP/paraffin samples with 20%, 40%, and 60% mass fraction of MOP were prepared, and electromagnetic properties were analyzed at 2–18 GHz using the coaxial method. The results show that 60 wt% sample has the best absorption performance, with a minimum reflection loss (RL$_{min}$) value of −22.06 dB at 15.04 GHz, and the effective absorption bandwidth (EAB, RL < −10 dB) reaches 4.16 GHz at a 7.65 mm absorber thickness, covering most of the Ku-band region. The excellent microwave absorption performance of MOP is due to its multi-oxide forming multi-interface structure and rough surface, which can not only form abundant dipole and interfacial polarization under the action of EMW, but also reflect and scatter the incident EMW, prolong the transmission path, and enhanced the absorption of microwaves. This study demonstrates that MOP building materials can have excellent microwave absorption properties, thus becoming a new way to address harmful manganese residue; for example, autoclaved bricks, which can not only improve the added value of manganese residue building materials but also can be consumed on a large scale. It provides a new idea to solve the harm of manganese residue.

Keywords: manganese ore powder (MOP); electromagnetic wave absorption; pollution control; dielectric loss

1. Introduction

Manganese is an important metal widely used in metallurgy, electronics, and the chemical industry [1]. With the sharp reduction in the grade of manganese ore brought about by long-term mining, the solid waste from manganese tailings mining has increased year by year [2]. At present, the main disposal method of manganese residue is stockpiling. However, the pollutants in manganese residue (such as Mn^{2+}, Cr^{6+}, Pd^{2+}, etc.) are easy to enter the water, soil, and air, destroy the ecological balance and endanger human health [3–5]. Meanwhile, long-term stockpiled manganese residue is easy to cause dam-break accidents. Therefore, to reduce ecological and environmental hazards, and promote the healthy development of the mining industry, research on the reduction, harmless, and resource utilization technology of manganese residue should be carried out.

Building materials are one of the main ways to consume manganese ore powder (MOP), which can be used to prepare roadbed, autoclaved brick, autoclaved aerated concrete, glass-ceramics, cement clinker, and geo-polymers, so as to realize the large-scale utilization of MOP [6–11]. For instance, Wang et al. [10] studied the mechanical and environmental properties of non-sintered permeable bricks prepared from electrolytic manganese residue (EMR). The test results showed that the splitting tensile strength of the optimal ratio (50 wt% of EMR) was 3.53 MPa, and the permeability coefficient was 3.2×10^{-2} cm/s. Li et al. [12] prepared autoclaved bricks with a filler mass fraction of 63% by EMR, which could be obtained with 1-day compressive strength of 23.5 MPa and the Mn leaching concentration of <0.02 mg·L^{-1}. Although researchers have carried out a large number of studies on resource utilization of manganese residue building materials, the overall combined utilization rate is low. Meanwhile, the increased costs associated with the pre-treatment of manganese residue have led to weak market competitiveness, which limits the promotion and application of manganese residue building materials. The motivation of this study is to find an effective way to improve the added value and large-scale utilization of MOP building materials.

Presently, with the development of electronic technology, it is vital to safeguard the electronic and information security of all types of ground buildings with important functions and tasks [13,14]. Researchers have worked to develop effective electromagnetic wave (EMW) shielding or EMW absorbing materials to solve these problems [15–18]. Wave absorbing materials exhibit greater advantages than shielding materials due to their ability to convert incident electromagnetic energy into thermal energy rather than reflecting it back into the environment [19–21]. Therefore, using building materials with high EMW absorption performance is a simple and effective way to realize electromagnetic protection for important ground buildings. Fortunately, the main components of MOP, such as SiO_2 [22], MnO [23], and Al_2O_3 [24], are typical dielectric loss microwave absorbing materials. This shows that MOP building materials, especially wall materials such as no-burn bricks, autoclaved bricks, non-sintered permeable bricks, and autoclaved aerated concrete with 30–60% admixture are expected to have an excellent electromagnetic absorption effect, which can not only consume a lot of manganese residue, but also improve the added value of MOP building materials. While, as far as we know, there are no published reports on the microwave absorption of MOP building materials.

To investigate the microwave absorption properties of manganese residue and its potential application in electromagnetic protection building materials, MOP was selected to explore the electromagnetic characteristics. Specifically, grind the MOP and fuse with flake paraffin, and then pressed into coaxial ring by mold to test and analyze electromagnetic parameters. Here, the filling mass fractions of 20%, 40% and 60% commonly used for manganese residue building materials are selected, and the experimental results show that the microwave absorption performance is positively correlated with the filling mass fraction. For the sample with 60 wt% mass fraction, the minimum reflection loss (RL$_{min}$) of −22.06 dB can be achieved at 15.04 GHz, and the effective absorption bandwidth (EAB, RL < −10 dB) of 4.16 GHz (13.84–18 GHz) can be obtained at a thickness of 7.65 mm. It is well known that the mass fraction of manganese residue filling suitable for autoclaved bricks should be greater than 60 wt%, and the thickness of the brick is usually 53 mm [12]. This shows that manganese residue building materials, especially autoclaved bricks, have excellent EMW absorption properties and can be used in electromagnetic protection buildings. In short, this study provides a brand new way to utilize manganese residue on a large scale and increase the added value of MOP building materials.

2. Experiment

2.1. Materials

The processing procedure for sample preparation is shown in Figure 1. Manganese ore was obtained from a typical manganese deposit in Xiushan County (Chongqing, China). The crushed manganese ore was dried in a constant temperature oven at 105 °C for 12 h,

and ground with a planetary ball mill for 12 h to obtain powder. Since the particle size of MOP used as construction raw material is generally around 150 μm, the powder obtained was passed through a 100 mesh sieve (particle size < 150 μm).
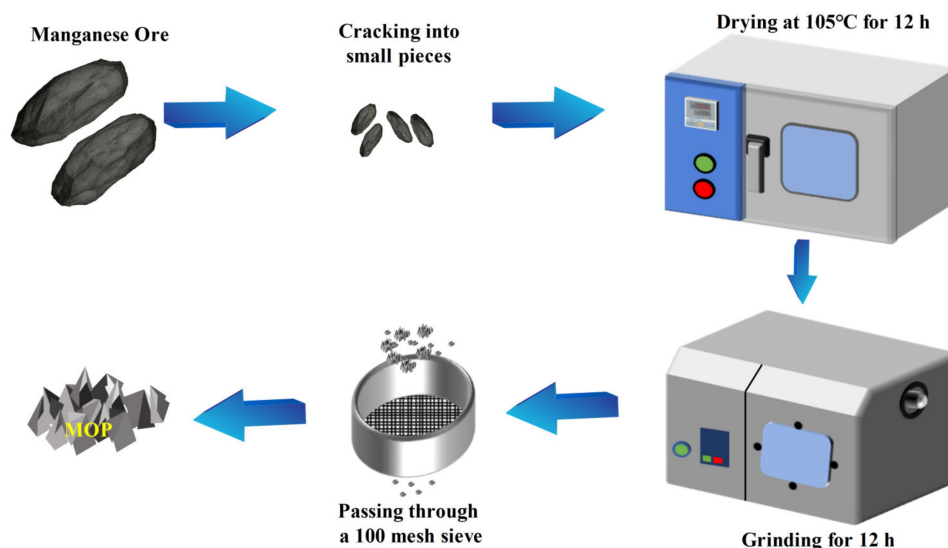
Figure 1. The preparation process of MOP.

2.2. Characterization

Elemental and chemical analyses were performed with X-ray fluorescence (XRF, AR-LAdvant'X Intellipower 3600, Waltham, MA, USA). The X-ray powder diffraction (XRD, Rigaku Ultima IV, Tokyo, Japan) method was carried out to identity the crystallization phase of the MOP, using nickel-filtered Cu Kα (λ = 0.154 nm) radiation at an angle of 5–85° at a scanning rate of 8 °/min. A scanning electron microscopy (FIB/SEM, ZEISS AURIGA, Oberkochen, Germany) with EDS equipment was used to observe the surface topography and elemental distribution of the MOP. The magnetic properties of the composites were measured with a vibrating sample magnetometer (VSM, LakeShore 7404, Columbus, OH, USA). The particle size distribution was analyzed with a laser particle size analyzer (PSA, Mastersizer 2000, Malvern, UK).

For the EMW absorption properties, the samples were prepared by mixing the MOP with melted paraffin at mass filling ratios of 20 wt%, 40 wt%, and 60 wt%, respectively. The mixture was compressed into a ring with an outer diameter of 7 mm, an inner diameter of 3.04 mm, and a thickness of 2.0 mm. The complex permittivity ($\varepsilon_r = \varepsilon' - j\varepsilon''$) and permeability ($\mu_r = \mu' - j\mu''$) were measured in the frequency range of 2.0–18.0 GHz using a vector network analyzer (VNA, Agilent N5244A, Santa Clara, CA, USA) with the coaxial line method.

3. Results and Discussion

3.1. Compositional and Microstructures of MOP

The particle size analysis graph of MOP is shown in Figure 2a. The average particle size in the sample was 61.351 μm, with particles smaller than 55.351 μm accounting for 50% of the total volume and particles smaller than 136.564 μm accounting for 90% of the total product. Overall, most of the crystals had particle sizes less than 150 μm. This meets the requirements for use as a raw material for the construction of building materials. In addition, the chemical composition of the materials was characterized by XRF. As shown in Figure 2b, the contents of SiO_2, Al_2O_3, Fe_2O_3, and CaO were 40.615%, 15.372%, 8.48%, and 3.905%, respectively, with a total content of 68.372%. It is noteworthy that these four are the main chemical components of the building materials [5].
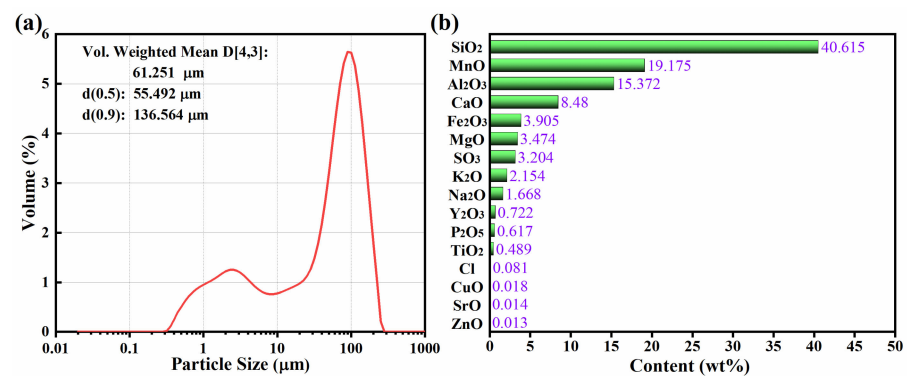
Figure 2. Particle size analysis (**a**) and chemical composition content (**b**) of MOP composite.

The physical phase analysis of MOP was measured to determine its applicability to the scenario. The results are shown in Figure 3. It can be seen that the four primary crystalline phases have the most obvious crystalline peaks, which are $KAL_2SI_3AlO_{10}(OH)_2$ (JCPDS:07-0025), $(K_{0.82}Na_{0.18})(Fe_{0.03}Al_{1.97})(AlSi_3)O_{10}(OH)_2$ (JCPDS:80-0742), $Mn(CO)_3$ (JCPDS:83-1763) and SiO_2 (JCPDS:99-0088). It is well known that quartz (SiO_2), muscovite ($KAl_2SI_3AlO_{10}(OH)_2$, $(K_{0.82}Na_{0.18})(Fe_{0.03}Al_{1.97})(AlSi_3)O_{10}(OH)_2$), and rhodochrosite ($Mn(CO)_3$) are necessary to obtain high-strength building materials. Therefore, MOP is a potential raw material for construction.
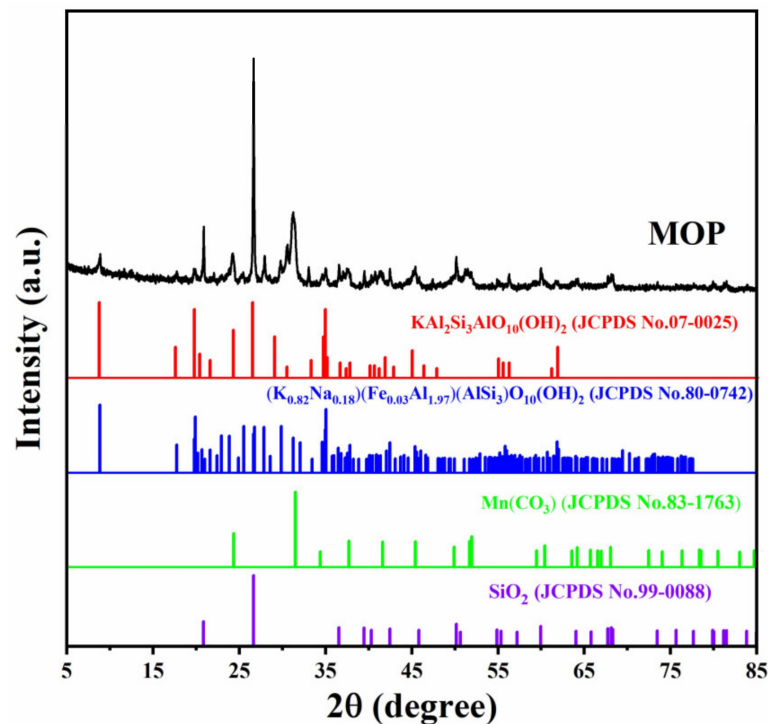

Figure 3. XRD patterns of MOP composite.

Figure 4 shows the field-emission scanning electron microscope (SEM) images of the MOP at different magnifications and the energy-dispersive X-ray spectra (EDS). The microscopic morphology of the same manganese ore powder composite at different magnifications, as shown in Figure 4a–c, indicates that the manganese ore powder composite has a diverse rough structure inside, specifically in the form of massive crystals, flake crystals, and a small number of powder crystals. The construction material based on this microstructure has excellent resistance to compression and friction. Additionally, it facilitates multiple reflections of EMW inside the absorber and thus extends the transmission path length, which helps to attenuate EMW [25].
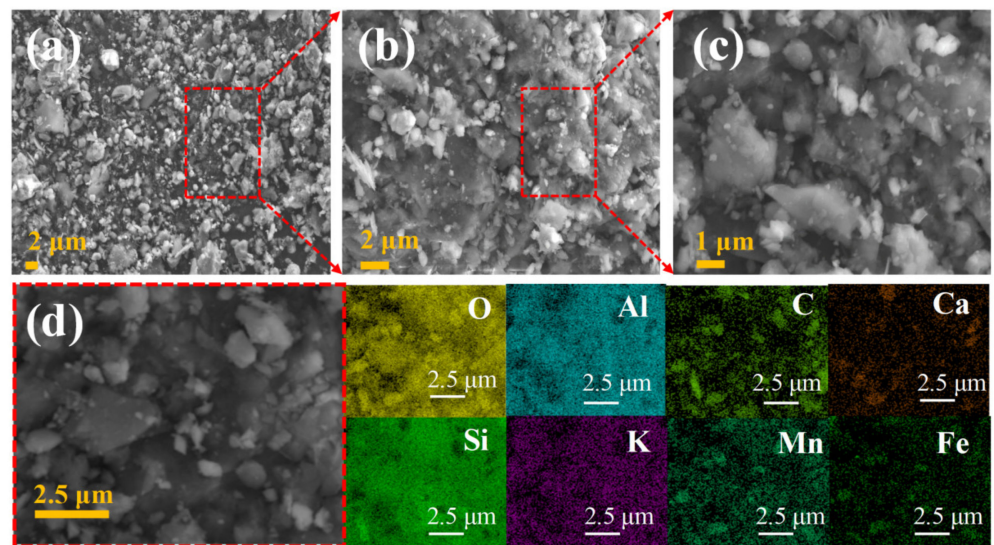
Figure 4. SEM images (**a**–**c**); element mapping (**d**) of MOP composite (O, Al, C, Ca, Si, K, Mn, Fe).

The EDS further confirms which atoms are contained in the MOP. Figure 4d shows the EDS elemental mapping of MOP, and it can be clearly observed that the manganese ore powder composites consist of O, Al, Si, K, C, Mn, Ca, and Fe in selected regions, which fits well with the XRF analysis results in Figure 2b. These elements may come from materials with microwave absorbing properties such as SiO_2, Al_2O_3, MnO, etc. Thus, it can be speculated that the MOP has relatively good EMW absorbing properties.

3.2. Electromagnetic Characteristics and Microwave Absorption Properties

Electromagnetic parameters (ε_r, μ_r) are the decisive factor for the microwave absorbing properties of materials, and the real parts of the permittivity and permeability (ε' and μ') indicate the storage capacity of electromagnetic energy, while the imaginary parts (ε'' and μ'') indicate the loss of electrical energy and magnetic loss, respectively [26–28].

Figure 5a,b shows the curves of ε' and ε'' values of MOP/paraffin wax samples at different filling rates, and all samples showed a similar trend; that is, with the increase of frequency, there is a decreasing trend. This phenomenon is due to the enhanced hysteresis of the polarization associated with the electric field variation at higher frequencies [29,30]. In addition, the increase in filling mass fraction leads to an increase in electrical conductivity, and thus, the complex permittivity increases with the increase in filling mass fraction [31,32]. Overall, the ε' and ε'' values of the MOP with three different filler mass fractions are almost constant over the entire frequency range. Moreover, ε'' shows multiple fluctuation peaks around 4, 9, 14 GHz, which demonstrates the occurrence of related polarization phenomena [33,34].

It is well known that dielectric losses consist of conduction losses, ion polarization, electron polarization, interfacial polarization, and dipole relaxation [35,36]. Electron polarization and ion polarization were not considered because these two are beyond the frequency range of our study (2–18 GHz) [37,38]. Therefore, interfacial polarization and dipole relaxation loss play a dominant role in the dielectric loss. To further explain the dielectric loss mechanism of MOP, the Debye dielectric relaxation model (Cole–Cole model) was used. According to the Debye dipolar relaxation theory, the relationship between ε' and ε'' can be expressed as [39,40]:

$$\left(\varepsilon' - \frac{\varepsilon_s + \varepsilon_\infty}{2} \right)^2 + (\varepsilon'')^2 = \left(\frac{\varepsilon_s - \varepsilon_\infty}{2} \right)^2 \tag{1}$$

where ε_s and ε_∞ are the static permittivity and relative dielectric permittivity at the high-frequency limit, respectively. As shown in Figure 6a–c, the manganese ore powder com-

posites all exhibited multiple strong and twisted semicircles at certain frequencies with the numbers 1, 2, and 4, respectively. It is demonstrated that multiple relaxation processes occurred within the material under the action of an applied electromagnetic field [33]. This is due to the complex structure of the MOP that causes the asymmetric distribution of space charges and generates a large number of defective dipoles, which leads to varying moments of relaxation loss [41,42]. Compared to dipole polarization, it tends to think that it is the interfacial polarization that contributes more because of its larger microscopic interface [43–45].
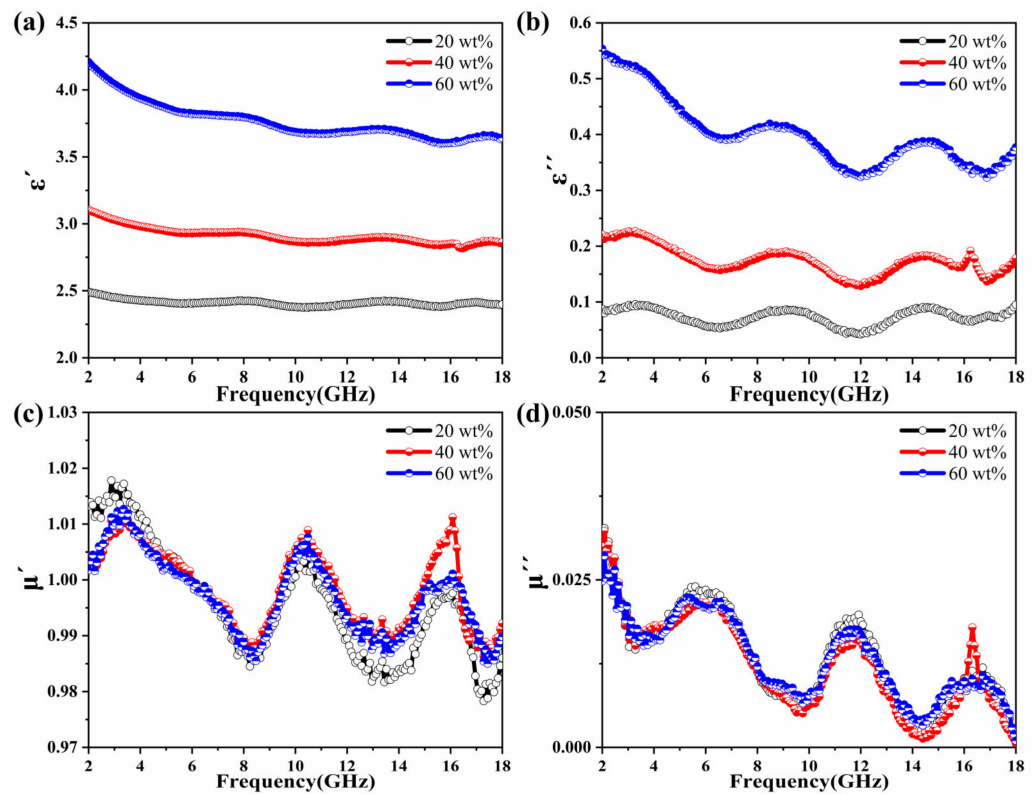
Figure 5. Frequency dependence of (**a**) real and (**b**) imaginary parts of complex permittivity, (**c**) real part, and (**d**) imaginary part of the relative complex permeability of the MOP composite with different filling ratios.
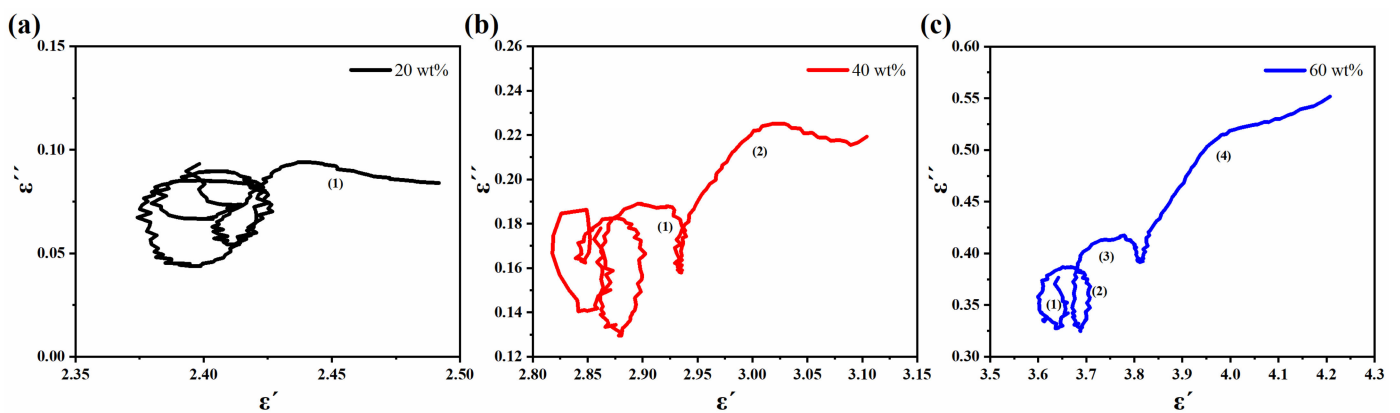
Figure 6. The relationship between the real part (ε') and imaginary part (ε'') of MOP composite material with 20 wt% loading (**a**), 40 wt% loading (**b**), and 60 wt% loading (**c**).

The curves of μ' and μ'' values of manganese ore powder composites with different filling ratios are shown in Figure 5c,d. From Figure 5c, it can be seen that the μ' values of

the three filling ratios show irregular fluctuations with the increase of frequency, and the fluctuation range is 1.01~0.97. The μ'' curve, on the other hand, fluctuates from 0.03 to 0. It is noteworthy that the μ' and μ'' values for the three different filling mass fractions almost overlap, which is because MOP contains only a small amount of metal particles that exhibit paramagnetism (Supplementary Materials; as shown in Figure S1). Therefore, as the filling mass fraction increases, the effect on the magnetic permeability is small. In short, the real (μ') and imaginary (μ'') parts of the samples for the three fill ratios are close to 1 and 0, respectively, which indicates relatively weak magnetic losses due to the natural magnetic resonance [46,47].

Magnetic losses in absorbing materials mainly originate from hysteresis, domain wall resonance, eddy current effects, natural resonance, and exchange resonance [48]. Hysteresis losses can be negligible due to the small applied electromagnetic field and domain wall resonance only occurs in multi-domain structural materials, usually in the megahertz range [25,49]. Therefore, the natural ferromagnetic resonance and the eddy current effects are two important parameters to be considered in this study. It is known that eddy current losses are related to the thickness and conductivity of the absorber and can be expressed by the following equation [50,51]:

$$\mu'' = 2\pi\mu_0 \left(\mu'\right)^2 \sigma d^2 f / 3 \tag{2}$$

$$C_0 = \mu'' \left(\mu'\right)^{-2} f^{-1} \tag{3}$$

where σ is the electrical conductivity, d is the sample thickness, and μ_0 denotes the magnetic permeability in a vacuum. If the magnetic loss originates from eddy current loss only, the value of C_0 should be a constant at varying frequencies. As shown in Figure 7, the value of C_0 for the three samples varies significantly over the entire frequency range, so it is not the magnetic loss caused by eddy current loss. In summary, the magnetic loss comes from the natural resonance and the exchange resonance. Noteworthy, the overall trend of C_0 value is decreasing and then stable, with only slight fluctuations at 5.1, 11.6, and 16.3 GHz. Since the natural resonance is generally lower than the exchange resonance frequency [52–54]. Therefore, the peak at 5.1 GHz is the natural resonance and the remaining two are the exchange resonance.
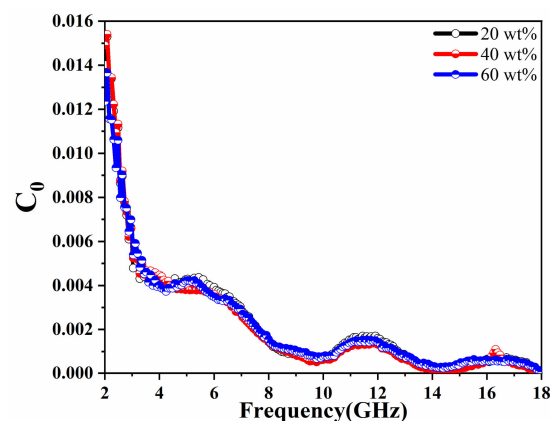
Figure 7. Eddy current loss (denoted by C_0) with frequency for MOP composite with different filling ratios.

It is known that the reflection loss (RL) can be used to evaluate the microwave absorption properties of a material. According to the transmission line theory of relative complex permittivity and magnetic permeability, the RL values can be calculated by the following equation [55–57]:

$$\text{RL}(dB) = 20\log|(Z_{in} - Z_0)/(Z_{in} + Z_0)| \tag{4}$$

where Z_0 is the free-space impedance of the absorber, and Z_{in} is the input impedance at the free space and material interface, which can be expressed as:

$$Z_{in} = Z_0 \sqrt{\mu_r/\varepsilon_r}\tanh[j(2\pi fd/c)\sqrt{\mu_r\varepsilon_r}] \tag{5}$$

where μ_r, ε_r are the relative complex permeability and relative complex permittivity; f is the frequency of microwave in free space, d is the thickness of absorber, and c is the speed of light.

Figure 8 shows the EMW absorption of samples with 20 wt%, 40 wt% and 60 wt% MOP in the frequency range of 2–18 GHz. From Figure 8a,c,e, it can be seen that MOP had good wave absorption performance, and the absorbing performance of the sample became better as the mass fraction of MOP filling increased (as also shown in Figure S2). For instance, as the filling mass fraction of MOP increased from 20% to 60%, the RL_{min} of the samples declined from −6.30 dB to −22.06 dB. Meanwhile, Figure 8b,d,f) shows the maximum EAB of the samples with 20 wt%, 40 wt%, and 60 wt% of MOP are 0, 1.68, and 4.16 GHz, respectively. In summary, the best EMW absorption performance of the samples was achieved when the filling mass fraction of MOP was 60 wt%, as shown by RL_{min} reaching −22.06 dB at 7.95 mm and EAB reaching 4.16 GHz at 7.65 mm.
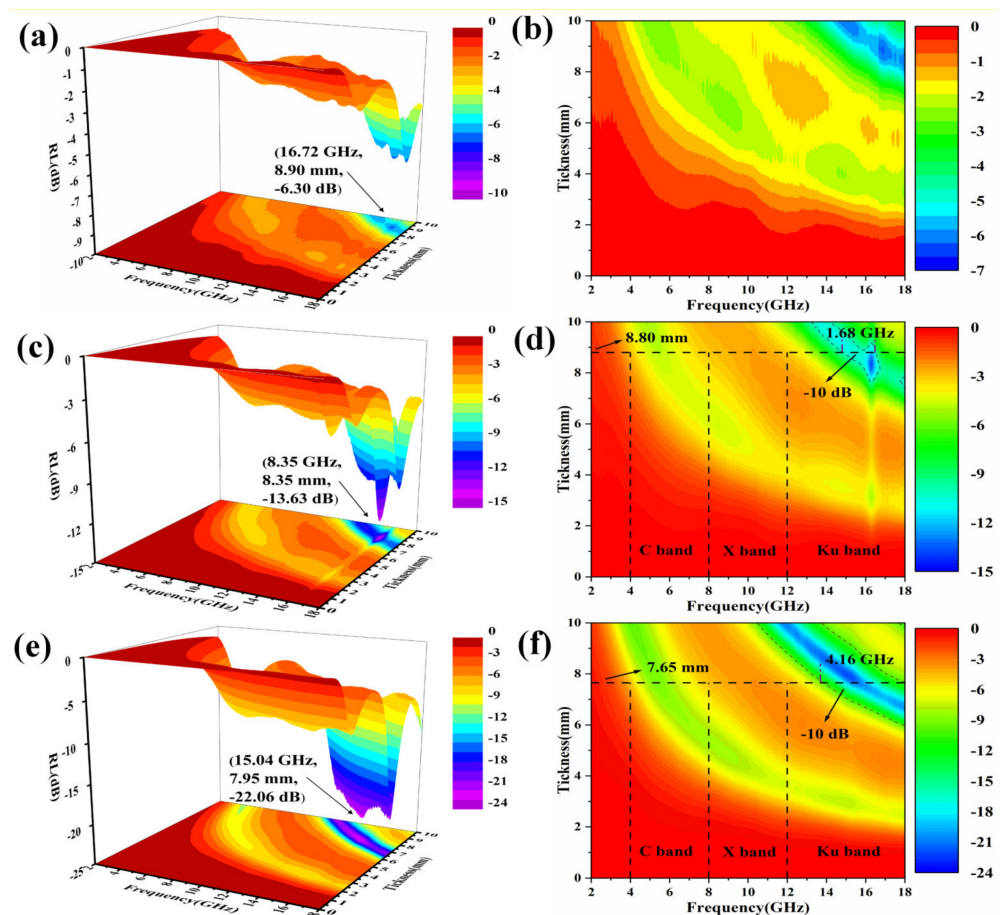
Figure 8. The 3D representation and contour plots of the reflection loss of MOP composite at different filling ratios: 20 wt% (**a,b**), 40 wt% (**c,d**), and 60 wt% (**e,f**).

This indicates that MOP with a filling mass fraction of 60 wt% has the best EMW absorption effect and is less than the thickness of 10 mm, while the autoclaved bricks usually require 60 wt% of MOP and a thickness of 53 mm [12,58]. It can be inferred that autoclaved bricks made from MOP have an excellent wave absorption effect and can

be used for electromagnetic protection building materials, thus realizing the large-scale utilization of MOP.

For comparison, the RL_{min} values and EAB curves of microwave absorption performance from the 3D contour plots in Figure 8 have been extracted and summarized in Figure 9. As shown in Figure 9a, the transformation trend of the RL_{min} value generally showed a gradual decrease with the increase in thickness. In contrast to the trend of RL_{min} values, the EAB values gradually increase with the increase of absorber thickness (Figure 9b). The samples with a filling mass fraction of 60 wt% exhibited good adsorption properties starting from a thickness of 6 mm. It is worth noting that this does not compound the thin thickness of traditional EMW absorbing materials, but the thickness of a standard autoclaved brick (53 mm) is much greater than this value. This further confirms that the application of MOP to autoclaved bricks is very suitable [59].
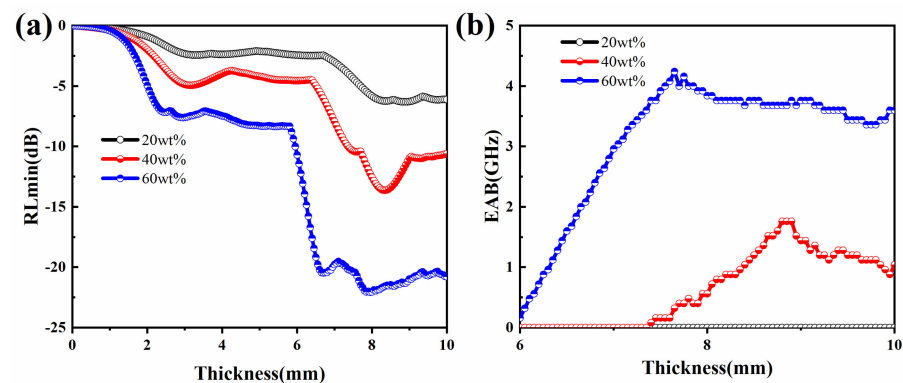

Figure 9. Absorber thickness dependence of (**a**) RLmin values, (**b**) EAB in composites with MOP.

Generally, relatively high attenuation constant (α) and well-matched impedance characteristics (Z_r) are two guarantees to have excellent absorption performance [60,61]. A high attenuation constant implies that a unit length of microwave absorbing material can convert more microwave energy into heat or interference [62,63]. The impedance matching determines the total amount of incident electromagnetic waves that can enter the material [64]. The two parameters mentioned above involved the following equations [65,66]:

$$\alpha = \frac{\sqrt{2}\pi f}{c} \times \sqrt{(\mu''\varepsilon'' - \mu'\varepsilon') + \sqrt{(\mu''\varepsilon'' - \mu'\varepsilon')^2 + (\mu'\varepsilon'' + \mu''\varepsilon')^2}} \qquad (6)$$

$$Z_r = \sqrt{\mu_r/\varepsilon_r} \qquad (7)$$

Figure 10a shows the attenuation constants of the MOP, the α of the three samples increases sharply with increasing frequency, indicating that these three samples have excellent attenuation ability in the high-frequency range. In the frequency range, the attenuation constants of the sample with 60 wt% of MOP are larger than those of the 40 wt% and the 20 wt% of samples, indicating that the sample with a filling mass fraction of 60 wt% has better attenuation performance. In addition, the exact impedance matching values of MOP composites as a function of frequency is given in Figure 10b, from which it can be seen that the specimens with different filler ratios deteriorate as the filler mass fraction increases. The larger the impedance matching value, the better the impedance matching characteristics, while 60 wt% of the sample has the worst impedance matching characteristics, which is due to the higher filler mass fraction, the better the conductivity. In summary, although the 60 wt% sample has poor impedance matching characteristics, it has the highest attenuation coefficient and therefore shows the best EMW absorption performance, which corresponds to the location of RL_{min} for the samples with different mass fractions in Figure 8.
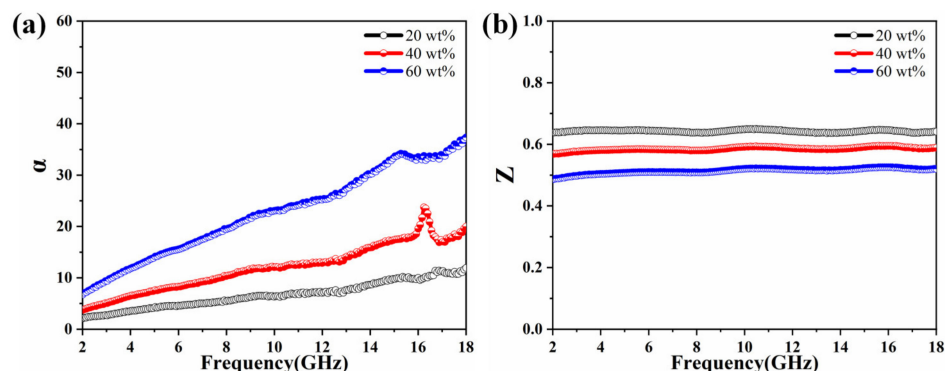
Figure 10. Frequency dependence of (**a**) attenuation constant α and (**b**) impedance matching Z for MOP composite with different filling ratios.

Figure 11 depicts in detail the EMW absorption mechanism of the MOP sample. Firstly, the multiple oxides such as SiO_2, Al_2O_3, and Fe_2O_3 in the sample lead to an asymmetric space charge distribution, which results in a large number of dipole polarization. Meanwhile, a large number of interfaces were generated between different oxides, which in turn leads to the occurrence of interfacial polarization. The dipole and interfacial polarization enhanced the attenuation of electromagnetic waves. Secondly, non-magnetic low-grade manganese residue showed a weak and almost constant magnetic loss, and the interfacial and dipole polarization proportional to the filling ratio brought about a significant increase in attenuation coefficient and microwave absorption capacity. Lastly, in the multilayer structure, multiple reflections and scattering occur between the abundant non-uniform interfaces and the randomly distributed chemical components, which prolongs the transmission path and facilitates the increase of EMW propagation path and energy attenuation, thus enhancing the absorption of EMW [67,68].
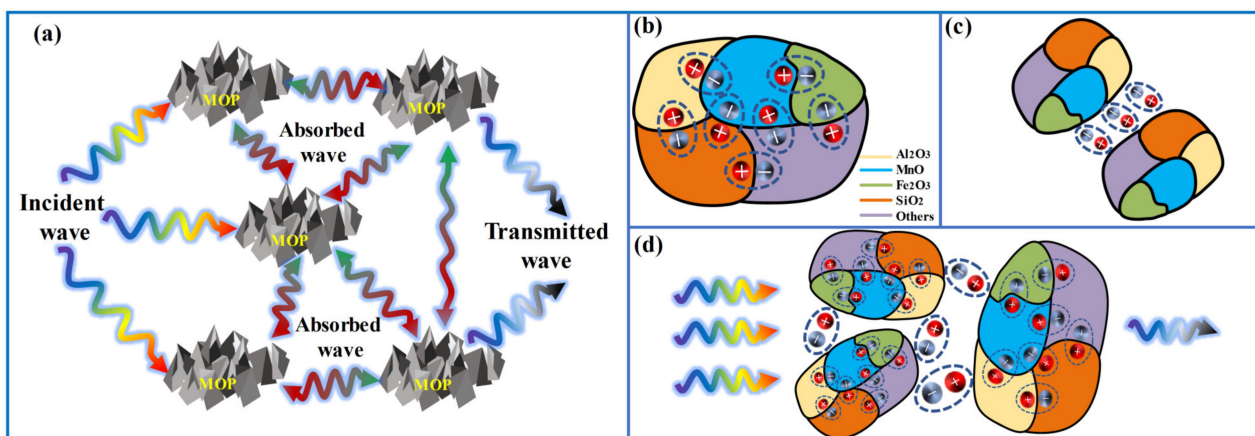
Figure 11. The EMW absorption mechanism of MOP: (**a**) multiple reflections, (**b**) dipole polarization, (**c**) interfacial polarization, and (**d**) dielectric and magnetic losses act in concert.

4. Conclusions

In this work, the EMW absorption performance of MOP is investigated. The EMW absorption performance of MOP/paraffin composites with different filling mass ratios (20 wt%, 40 wt%, and 60 wt%) was tested and analyzed in the range of 2–18 GHz. When the filling mass fraction is 60 wt% with an absorber thickness of 7.95 mm, the RL_{min} value reaches -22.06 dB at 7.53 GHz, and the widest EAB reaches 4.16 GHz at a 7.65 mm absorber thickness, covering most of the Ku-band region. This excellent broadband absorption performance is attributed to the dipole polarization and interfacial polarization due to the multi-oxide of the MOP. In addition, the multi-interface structure and rough surface

composed of multi-oxide can effectively reflect and scatter the incident electromagnetic wave, prolong the transmission path and enhance the absorption of electromagnetic wave.

It is well known that building materials, such as autoclaved bricks, usually need to be filled with more than 60 wt% manganese residue, and the thickness is 53 mm. Thus it can be seen that the research in this paper provides a new and effective way to realize the resource utilization of manganese, which will alleviate the ecological and environmental risks caused by large amounts of stockpiles, crack the problem of low value-added MOP, and its application in building materials can realize absorbing broadband electromagnetic shielding buildings.

Supplementary Materials: The following supporting information can be downloaded at https://www.mdpi.com/article/10.3390/molecules27123758/s1, Figure S1: Magnetic hysteresis loops of MOP.; Figure S2: Frequency dependence of (**a**) absorption and (**b**) transmission of MOP composites with different filling ratios.

Author Contributions: Conceptualization, Y.Z.; data curation, R.C., J.R. and X.H.; formal analysis, W.Z.; funding acquisition, P.Y.; investigation, P.Y., K.Y. and Z.D.; methodology, W.Z., Z.D., P.Y. and Y.Z.; project administration, Y.Z.; software, X.H.; validation, W.Z. and Z.D.; visualization, D.W.; writing—original draft, R.C. and W.Z.; writing—review and editing, P.Y., K.Y. and Y.Z. All authors have read and agreed to the published version of the manuscript.

Data Availability Statement: The date of the compounds are available from the authors.

Conflicts of Interest: The authors declare no conflict of interest.

Sample Availability: Samples of the compounds are available from the authors.

References

1. Camargo, F.P.; do Prado, P.F.; Tonello, P.S.; Dos Santos, A.C.A.; Duarte, I.C.S. Bioleaching of Toxic Metals from Sewage Sludge by Co-Inoculation of Acidithiobacillus and the Biosurfactant-Producing Yeast Meyerozyma Guilliermondii. *J. Environ. Manag.* **2018**, *211*, 28–35. [CrossRef] [PubMed]
2. Liu, T.; Wu, K.; Zeng, L. Removal of Phosphorus by a Composite Metal Oxide Adsorbent Derived from Manganese Ore Tailings. *J. Hazard. Mater.* **2012**, *217–218*, 29–35. [CrossRef] [PubMed]
3. Okereafor, U.; Makhatha, M.; Mekuto, L.; Uche-Okereafor, N.; Sebola, T.; Mavumengwana, V. Toxic Metal Implications on Agricultural Soils, Plants, Animals, Aquatic Life and Human Health. *Int. J. Environ. Res. Public Health* **2020**, *17*, 2204. [CrossRef]
4. Song, J.; Yang, X.; Chen, P.; Liu, R.; Luo, D.; Li, J.; Liu, J. Sintering Technology and Properties of Permeable Bricks Prepared Using Manganese Tailings. *J. Ceram. Processing Res.* **2021**, *22*, 283–288. [CrossRef]
5. He, D.; Shu, J.; Wang, R.; Chen, M.; Wang, R.; Gao, Y.; Liu, R.; Liu, Z.; Xu, Z.; Tan, D.; et al. A Critical Review on Approaches for Electrolytic Manganese Residue Treatment and Disposal Technology: Reduction, Pretreatment, and Reuse. *J. Hazard. Mater.* **2021**, *418*, 126235. [CrossRef] [PubMed]
6. Liang, D.Q.; Qin, F.; Jiang, J.B. Road Performance of Concrete Incorporating Manganese Slag. *Adv. Mater. Res.* **2011**, *402*, 457–462. [CrossRef]
7. Miao, X.; Bai, Z.; Qiu, G.; Tang, S.; Guo, M.; Cheng, F.; Zhang, M. Preparation of Transparent Mn-Doped CaF_2 Glass-Ceramics from Silicon-Manganese Slag: Dependence of Colour-Controllable Change on Slag Addition and Crystallization Behavior. *J. Eur. Ceram. Soc.* **2020**, *40*, 3249–3261. [CrossRef]
8. Navarro, R.; Alcocel, E.G.; Sánchez, I.; Garcés, P.; Zornoza, E. Mechanical Properties of Alkali Activated Ground SiMn Slag Mortars with Different Types of Aggregates. *Constr. Build. Mater.* **2018**, *186*, 79–89. [CrossRef]
9. Wang, P.; Liu, D. Preparation of Baking-Free Brick from Manganese Residue and Its Mechanical Properties. *J. Nanomater.* **2013**, *2013*, 1–5. [CrossRef]
10. Wang, Y.; Gao, S.; Liu, X.; Tang, B.; Mukiza, E.; Zhang, N. Preparation of Non-Sintered Permeable Bricks Using Electrolytic Manganese Residue: Environmental and NH_3-N Recovery Benefits. *J. Hazard. Mater.* **2019**, *378*, 120768. [CrossRef]
11. Tang, B.; Gao, S.; Wang, Y.; Liu, X.; Zhang, N. Pore Structure Analysis of Electrolytic Manganese Residue Based Permeable Brick by Using Industrial CT. *Constr. Build. Mater.* **2019**, *208*, 697–709. [CrossRef]

12. Li, J.; Lv, Y.; Jiao, X.; Sun, P.; Li, J.; Wuri, L.; Zhang, T.C. Electrolytic Manganese Residue Based Autoclaved Bricks with Ca(OH)$_2$ and Thermal-Mechanical Activated K-Feldspar Additions. *Constr. Build. Mater.* **2020**, *230*, 116848. [CrossRef]

13. Yang, P.-A.; Huang, Y.; Li, R.; Huang, X.; Ruan, H.; Shou, M.; Li, W.; Zhang, Y.; Li, N.; Dong, L. Optimization of Fe@Ag Core–Shell Nanowires with Improved Impedance Matching and Microwave Absorption Properties. *Chem. Eng. J.* **2022**, *430*, 132878. [CrossRef]

14. Ma, L.; Li, S.; Liu, F.; Ma, S.; Han, E.-H.; Zhang, Z. Metal-Organic Framework-Derived Co/C Composite with High Magnetization as Broadband Electromagnetic Wave Absorber. *J. Alloys Compd.* **2022**, *906*, 164257. [CrossRef]

15. Plyushch, A.; Macutkevic, J.; Svirskas, S.; Banys, J.; Plausinaitiene, V.; Bychanok, D.; Maksimenko, S.A.; Selskis, A.; Sokal, A.; Lapko, K.N.; et al. Silicon Carbide/Phosphate Ceramics Composite for Electromagnetic Shielding Applications: Whiskers vs Particles. *Appl. Phys. Lett.* **2019**, *114*, 183105. [CrossRef]

16. Spinelli, G.; Lamberti, P.; Tucci, V.; Kotsilkova, R.; Ivanov, E.; Menseidov, D.; Naddeo, C.; Romano, V.; Guadagno, L.; Adami, R.; et al. Nanocarbon/Poly(Lactic) Acid for 3D Printing: Effect of Fillers Content on Electromagnetic and Thermal Properties. *Materials* **2019**, *12*, 2369. [CrossRef]

17. Jiao, Y.; Song, Q.; Yin, X.; Han, L.; Li, W.; Li, H. Grow Defect-Rich Bamboo-like Carbon Nanotubes on Carbon Black for Enhanced Microwave Absorption Properties in X Band. *J. Mater. Sci. Technol.* **2022**, *119*, 200–208. [CrossRef]

18. Qian, J.; Shui, A.; Du, B.; Cai, M.; He, C.; Zeng, S.; Zhong, X.; Lou, J. Synthesis and Tunable Electromagnetic Shielding and Absorption Performance of the Three-Dimensional SiC Nanowires/Carbon Fiber Composites. *J. Eur. Ceram. Soc.* **2022**, *42*, 4154–4161. [CrossRef]

19. Meisak, D.; Gurnevich, E.; Plyushch, A.; Bychanok, D.; Georgiev, V.; Kotsilkova, R.; Kuzhir, P. Robust Design of Compact Microwave Absorbers and Waveguide Matched Loads Based on DC-Conductive 3D-Printable Filament. *J. Phys. D Appl. Phys.* **2020**, *53*, 305301. [CrossRef]

20. Yun, T.; Kim, H.; Iqbal, A.; Cho, Y.S.; Lee, G.S.; Kim, M.; Kim, S.J.; Kim, D.; Gogotsi, Y.; Kim, S.O.; et al. Electromagnetic Shielding of Monolayer MXene Assemblies. *Adv. Mater.* **2020**, *32*, 1906769. [CrossRef]

21. Wang, Y.; Yao, L.; Zheng, Q.; Cao, M.-S. Graphene-Wrapped Multiloculated Nickel Ferrite: A Highly Efficient Electromagnetic Attenuation Material for Microwave Absorbing and Green Shielding. *Nano Res.* **2022**, 1–10. [CrossRef]

22. Wen, G.; Wu, G.L.; Lei, T.Q.; Zhou, Y.; Guo, Z.X. Co-Enhanced SiO$_2$-BN Ceramics for High-Temperature Dielectric Applications. *J. Eur. Ceram. Soc.* **2000**, *20*, 1923–1928. [CrossRef]

23. Xu, D.; Qiao, J.; Wu, N.; Liu, W.; Wang, F.; Lv, L.; Pan, J.; Dong, Y.; Liu, J. Facile Synthesis of Three-Dimensional Porous Co/MnO Composites Derived from Bimetal Oxides for Highly Efficient Electromagnetic Wave Absorption. *ACS Sustain. Chem. Eng.* **2019**, *33*, 8687–8695. [CrossRef]

24. Mei, H.; Yang, D.; Yang, W.; Yao, L.; Yao, Y.; Cheng, L.; Zhang, L. 3D-Printed Impedance Gradient Al$_2$O$_3$ Ceramic with in-Situ Growing Needle-like SiC Nanowires for Electromagnetic Wave Absorption. *Ceram. Int.* **2021**, *47*, 31990–31999. [CrossRef]

25. Lu, Y.; You, W.; Cai, C.; Yu, X.; Zhao, Y.; Liu, X.; Guo, J.; Zhang, X.; Zeng, W.; Che, R. Insights into the Micro Magnetic Loss Mechanism of Microwave Absorption by Off-Axis Electron Holography. *J. Magn. Magn. Mater.* **2019**, *475*, 24–29. [CrossRef]

26. Zhao, H.; Cheng, Y.; Lv, H.; Ji, G.; Du, Y. A Novel Hierarchically Porous Magnetic Carbon Derived from Biomass for Strong Lightweight Microwave Absorption. *Carbon* **2019**, *142*, 245–253. [CrossRef]

27. Lü, Y.; Wang, Y.; Li, H.; Lin, Y.; Jiang, Z.; Xie, Z.; Kuang, Q.; Zheng, L. MOF-Derived Porous Co/C Nanocomposites with Excellent Electromagnetic Wave Absorption Properties. *ACS Appl. Mater. Interfaces* **2015**, *7*, 13604–13611. [CrossRef]

28. Han, M.; Yin, X.; Duan, W.; Ren, S.; Zhang, L.; Cheng, L. Hierarchical Graphene/SiC Nanowire Networks in Polymer-Derived Ceramics with Enhanced Electromagnetic Wave Absorbing Capability. *J. Eur. Ceram. Soc.* **2016**, *36*, 2695–2703. [CrossRef]

29. Yin, Y.; Liu, X.; Wei, X.; Yu, R.; Shui, J. Porous CNTs/Co Composite Derived from Zeolitic Imidazolate Framework: A Lightweight, Ultrathin, and Highly Efficient Electromagnetic Wave Absorber. *ACS Appl. Mater. Interfaces* **2016**, *8*, 34686–34698. [CrossRef]

30. Song, C.; Yin, X.; Han, M.; Li, X.; Hou, Z.; Zhang, L.; Cheng, L. Three-Dimensional Reduced Graphene Oxide Foam Modified with ZnO Nanowires for Enhanced Microwave Absorption Properties. *Carbon* **2017**, *116*, 50–58. [CrossRef]

31. Lai, Y.; Lv, L.; Fu, H. Preparation and Study of Al$_2$O$_3$@PPy@rGO Composites with Microwave Absorption Properties. *J. Alloys Compd.* **2020**, *832*, 152957. [CrossRef]

32. He, J.; Gao, S.; Zhang, Y.; Zhang, X.; Li, H. N-Doped Residual Carbon from Coal Gasification Fine Slag Decorated with Fe$_3$O$_4$ Nanoparticles for Electromagnetic Wave Absorption. *J. Mater. Sci. Technol.* **2022**, *104*, 98–108. [CrossRef]

33. Du, Y.; Liu, W.; Qiang, R.; Wang, Y.; Han, X.; Ma, J.; Xu, P. Shell Thickness-Dependent Microwave Absorption of Core–Shell Fe$_3$O$_4$@C Composites. *ACS Appl. Mater. Interfaces* **2014**, *6*, 12997–13006. [CrossRef]

34. Xiong, J.; Xiang, Z.; Zhao, J.; Yu, L.; Cui, E.; Deng, B.; Liu, Z.; Liu, R.; Lu, W. Layered NiCo Alloy Nanoparticles/Nanoporous Carbon Composites Derived from Bimetallic MOFs with Enhanced Electromagnetic Wave Absorption Performance. *Carbon* **2019**, *154*, 391–401. [CrossRef]

35. Yan, L.; Liu, J.; Zhao, S.; Zhang, B.; Gao, Z.; Ge, H.; Chen, Y.; Cao, M.; Qin, Y. Coaxial Multi-Interface Hollow Ni-Al$_2$O$_3$-ZnO Nanowires Tailored by Atomic Layer Deposition for Selective-Frequency Absorptions. *Nano Res.* **2017**, *10*, 1595–1607. [CrossRef]

36. Sun, G.; Dong, B.; Cao, M.; Wei, B.; Hu, C. Hierarchical Dendrite-Like Magnetic Materials of Fe$_3$O$_4$, γ-Fe$_2$O$_3$, and Fe with High Performance of Microwave Absorption. *Chem. Mater.* **2011**, *23*, 1587–1593. [CrossRef]

37. Zhang, Y.; Huang, Y.; Zhang, T.; Chang, H.; Xiao, P.; Chen, H.; Huang, Z.; Chen, Y. Broadband and Tunable High-Performance Microwave Absorption of an Ultralight and Highly Compressible Graphene Foam. *Adv. Mater.* **2015**, *27*, 2049–2053. [CrossRef]

38. Chen, C.; Bao, S.; Zhang, B.; Chen, Y.; Chen, W.; Wang, C. Coupling Fe@Fe$_3$O$_4$ Nanoparticles with Multiple-Walled Carbon Nanotubes with Width Band Electromagnetic Absorption Performance. *Appl. Surf. Sci.* **2019**, *467–468*, 836–843. [CrossRef]

39. Bai, B.; Zhu, Y.; Miao, J.; Wang, X.; Bi, S.; Kong, L.; Liu, W.; Zhang, L. Electromagnetic Wave Absorption Performance and Mechanisms of Geoploymer-Based Composites Containing Core-Shell SiO$_2$@Fe$_3$O$_4$ Nanoparticles. *Ceram. Int.* **2022**, *48*, 2755–2762. [CrossRef]

40. Wang, Y.; Di, X.; Lu, Z.; Cheng, R.; Wu, X.; Gao, P. Controllable Heterogeneous Interfaces of Cobalt/Carbon Nanosheets/RGO Composite Derived from Metal-Organic Frameworks for High-Efficiency Microwave Attenuation. *Carbon* **2022**, *187*, 404–414. [CrossRef]

41. Lv, H.; Zhou, X.; Wu, G.; Kara, U.I.; Wang, X. Engineering Defects in 2D G-C$_3$N$_4$ for Wideband, Efficient Electromagnetic Absorption at Elevated Temperature. *J. Mater. Chem. A* **2021**, *9*, 19710–19718. [CrossRef]

42. Wu, F.; Li, Q.; Liu, Z.; Shah, T.; Ahmad, M.; Zhang, Q.; Zhang, B. Fabrication of Binary MOF-Derived Hybrid Nanoflowers via Selective Assembly and Their Microwave Absorbing Properties. *Carbon* **2021**, *182*, 484–496. [CrossRef]

43. Ge, J.; Liu, L.; Cui, Y.; Li, R.; Meng, F.; Wang, F. Optimizing the Electromagnetic Wave Absorption Performances of Designed Fe$_3$O$_4$@SiO$_2$@MnO$_2$ Hybrids. *Ceram. Int.* **2020**, *46*, 15325–15332. [CrossRef]

44. Yang, J.; Shen, Z.; Hao, Z. Microwave Characteristics of Sandwich Composites with Mesophase Pitch Carbon Foams as Core. *Carbon* **2004**, *42*, 1882–1885. [CrossRef]

45. Guo, X.; Lu, J.; Liu, J.; Liu, C.; Tong, Y.; Li, J.; Sun, H.; Peng, H.; Wu, S.; Feng, Y.; et al. Enhanced Electromagnetic Wave Absorption Properties of PDCs-SiCN(Ni) Fibers by in-Situ Formed CNTs and Ni$_2$Si. *Ceram. Int.* **2022**, *48*, 20495–20505. [CrossRef]

46. Wu, Z.; Qian, X.; Pei, K.; You, W.; Li, X.; Jin, C.; Che, R. Drawing Advanced Electromagnetic Functional Composites with Ultra-Low Filler Loading. *Chem. Eng. J.* **2020**, *399*, 125720. [CrossRef]

47. Zhao, Y.; Zuo, X.; Guo, Y.; Huang, H.; Zhang, H.; Wang, T.; Wen, N.; Chen, H.; Cong, T.; Muhammad, J.; et al. Structural Engineering of Hierarchical Aerogels Comprised of Multi-Dimensional Gradient Carbon Nanoarchitectures for Highly Efficient Microwave Absorption. *Nano-Micro Lett.* **2021**, *13*, 144. [CrossRef]

48. Lu, B.; Dong, X.L.; Huang, H.; Zhang, X.F.; Zhu, X.G.; Lei, J.P.; Sun, J.P. Microwave Absorption Properties of the Core/Shell-Type Iron and Nickel Nanoparticles. *J. Magn. Magn. Mater.* **2008**, *320*, 1106–1111. [CrossRef]

49. Wu, M.; Zhang, Y.D.; Hui, S.; Xiao, T.D.; Ge, S.; Hines, W.A.; Budnick, J.I.; Taylor, G.W. Microwave Magnetic Properties of Co$_{50}$/(SiO$_2$)$_{50}$ Nanoparticles. *Appl. Phys. Lett.* **2002**, *80*, 4404–4406. [CrossRef]

50. Wang, K.; Chen, Y.; Tian, R.; Li, H.; Zhou, Y.; Duan, H.; Liu, H. Porous Co–C Core–Shell Nanocomposites Derived from Co-MOF-74 with Enhanced Electromagnetic Wave Absorption Performance. *ACS Appl. Mater. Interfaces* **2018**, *10*, 11333–11342. [CrossRef]

51. Lu, Z.; Wang, Y.; Di, X.; Cheng, R.; Yang, L.; Gao, P. Design of Hierarchical Core-Shell ZnFe$_2$O$_4$@MnO$_2$@RGO Composite with Heterogeneous Interfaces for Enhanced Microwave Absorption. *Ceram. Int.* **2022**, *48*, 5217–5228. [CrossRef]

52. Fu, L.-S.; Jiang, J.-T.; Xu, C.-Y.; Zhen, L. Synthesis of Hexagonal Fe Microflakes with Excellent Microwave Absorption Performance. *CrystEngComm* **2012**, *14*, 6827. [CrossRef]

53. Wang, H.; Dai, Y.; Gong, W.; Geng, D.; Ma, S.; Li, D.; Liu, W.; Zhang, Z. Broadband Microwave Absorption of CoNi@C Nanocapsules Enhanced by Dual Dielectric Relaxation and Multiple Magnetic Resonances. *Appl. Phys. Lett.* **2013**, *102*, 223113. [CrossRef]

54. Cao, M.-S.; Cai, Y.-Z.; He, P.; Shu, J.-C.; Cao, W.-Q.; Yuan, J. 2D MXenes: Electromagnetic Property for Microwave Absorption and Electromagnetic Interference Shielding. *Chem. Eng. J.* **2019**, *359*, 1265–1302. [CrossRef]

55. Chen, D.; Wang, G.-S.; He, S.; Liu, J.; Guo, L.; Cao, M.-S. Controllable Fabrication of Mono-Dispersed RGO–Hematite Nanocomposites and Their Enhanced Wave Absorption Properties. *J. Mater. Chem. A* **2013**, *1*, 5996. [CrossRef]

56. Huang, B.; Yue, J.; Wei, Y.; Huang, X.; Tang, X.; Du, Z. Enhanced Microwave Absorption Properties of Carbon Nanofibers Functionalized by FeCo Coatings. *Appl. Surf. Sci.* **2019**, *483*, 98–105. [CrossRef]

57. Gao, S.; Zhang, Y.; Xing, H.; Li, H. Controlled Reduction Synthesis of Yolk-Shell Magnetic@void@C for Electromagnetic Wave Absorption. *Chem. Eng. J.* **2020**, *387*, 124149. [CrossRef]

58. Ahmari, S.; Zhang, L. Durability and Leaching Behavior of Mine Tailings-Based Geopolymer Bricks. *Constr. Build. Mater.* **2013**, *44*, 743–750. [CrossRef]

59. Du, B.; Zhou, C.; Duan, N. Recycling of Electrolytic Manganese Solid Waste in Autoclaved Bricks Preparation in China. *J. Mater. Cycles Waste Manag.* **2014**, *16*, 258–269. [CrossRef]

60. Li, X.; Feng, J.; Du, Y.; Bai, J.; Fan, H.; Zhang, H.; Peng, Y.; Li, F. One-Pot Synthesis of CoFe$_2$O$_4$/Graphene Oxide Hybrids and Their Conversion into FeCo/Graphene Hybrids for Lightweight and Highly Efficient Microwave Absorber. *J. Mater. Chem. A* **2015**, *3*, 5535–5546. [CrossRef]

61. Wang, C.; Han, X.; Xu, P.; Zhang, X.; Du, Y.; Hu, S.; Wang, J.; Wang, X. The Electromagnetic Property of Chemically Reduced Graphene Oxide and Its Application as Microwave Absorbing Material. *Appl. Phys. Lett.* **2011**, *98*, 072906. [CrossRef]

62. Wang, C.; Murugadoss, V.; Kong, J.; He, Z.; Mai, X.; Shao, Q.; Chen, Y.; Guo, L.; Liu, C.; Angaiah, S.; et al. Overview of Carbon Nanostructures and Nanocomposites for Electromagnetic Wave Shielding. *Carbon* **2018**, *140*, 696–733. [CrossRef]

63. Kuang, J.; Jiang, P.; Ran, F.; Cao, W. Conductivity-Dependent Dielectric Properties and Microwave Absorption of Al-Doped SiC Whiskers. *J. Alloys Compd.* **2016**, *687*, 227–231. [CrossRef]

64. Wang, C.; Chen, L.; He, H.; Ye, T.; Deng, Q.; Wei, H.; Zhao, F.; Wang, Q. Nano-SiC-Decorated Y$_2$Si$_2$O$_7$ Ceramic for Enhancing Electromagnetic Waves Absorption Performance. *Ceram. Int.* **2022**, *48*, 20168–20175. [CrossRef]

65. Cao, M.; Wang, X.; Cao, W.; Fang, X.; Wen, B.; Yuan, J. Thermally Driven Transport and Relaxation Switching Self-Powered Electromagnetic Energy Conversion. *Small* **2018**, *14*, 1800987. [CrossRef]

66. Wang, P.; Cheng, L.; Zhang, Y.; Zhang, L. Flexible SiC/Si_3N_4 Composite Nanofibers with in Situ Embedded Graphite for Highly Efficient Electromagnetic Wave Absorption. *ACS Appl. Mater. Interfaces* **2017**, *9*, 28844–28858. [CrossRef]

67. Chen, Y.-J.; Xiao, G.; Wang, T.-S.; Ouyang, Q.-Y.; Qi, L.-H.; Ma, Y.; Gao, P.; Zhu, C.-L.; Cao, M.-S.; Jin, H.-B. Porous $Fe_3O_4/Carbon$ Core/Shell Nanorods: Synthesis and Electromagnetic Properties. *J. Phys. Chem. C* **2011**, *115*, 13603–13608. [CrossRef]

68. Zhao, B.; Guo, X.; Zhao, W.; Deng, J.; Fan, B.; Shao, G.; Bai, Z.; Zhang, R. Facile Synthesis of Yolk–Shell Ni@void@SnO2(Ni_3Sn_2) Ternary Composites via Galvanic Replacement/Kirkendall Effect and Their Enhanced Microwave Absorption Properties. *Nano Res.* **2017**, *10*, 331–343. [CrossRef]